Hindawi
Wireless Communications and Mobile Computing
Volume 2020, Article ID 8851600, 13 pages
https://doi.org/10.1155/2020/8851600

Research Article

Measurement and Simulation for Vehicle-to-Infrastructure Communications at 3.5 GHz for 5G

Yi Zeng,[1] **Haofan Yi**,[2,3] **Zijie Xia**,[2,3] **Shaoshi Wang**,[2,3] **Bo Ai**,[2,3] **Dan Fei**,[2,3] **Weidan Li**,[1] **and Ke Guan**[2,3]

[1]*Guangdong Communications & Networks Institute, 510700 Guangzhou, China*
[2]*State Key Laboratory of Rail Traffic Control and Safety, Beijing Jiaotong University, 100044 Beijing, China*
[3]*Beijing Engineering Research Center of High-Speed Railway Broadband Mobile Communications, Beijing, China*

Correspondence should be addressed to Haofan Yi; haofanyi@bjtu.edu.cn

Received 28 July 2020; Revised 21 August 2020; Accepted 17 November 2020; Published 15 December 2020

Academic Editor: Zhipeng Cai

Intelligent Transportation System (ITS) is more and more crucial in the modern transportation field, such as the applications of autonomous vehicles, dynamic traffic light sequences, and automatic road enforcement. As the upcoming fifth-generation mobile network (5G) is entering the deployment phase, the idea of cellular vehicle-to-everything (C-V2X) is proposed. The same 5G networks, coming to mobile phones, will also allow vehicles to communicate wirelessly with each other. Hence, 3.5 GHz, as the main sub-6 GHz band licensed in 5G, is focused in our study. In this paper, a comprehensive study on the channel characteristics for vehicle-to-infrastructure (V2I) link at 3.5 GHz frequency band is conducted through channel measurements and ray-tracing (RT) simulations. Firstly, the channel parameters of the V2I link are characterized based on the measurements, including power delay profile (PDP), path loss, root-mean-square (RMS) delay spread, and coherence bandwidth. Then, the measurement-validated RT simulator is utilized to conduct the simulations in order to supplement other channel parameters, in terms of the Ricean *K*-factor, angular spreads, the cross-correlations of abovementioned parameters, and the autocorrelation of each parameter itself. This work is aimed at helping the researchers understand the channel characteristics of the V2I link at 3.5 GHz and support the link-level and system level design for future vehicular communications of 5G.

1. Introduction

Intelligent Transportation System (ITS) is more and more crucial in the modern transportation field, such as the applications of autonomous vehicles, dynamic traffic light sequences, and automatic road enforcement. Since the vehicles are at high speed, the real-time and fast exchange of dynamic information should be transmitted in a short time from vehicle-to-everything (V2X) [1]. The V2X provides wireless services for vehicle-to-vehicle (V2V), vehicle-to-infrastructure (V2I), and vehicle-to-pedestrian (V2P) communications. Such transferred information includes not only small data such as the speed, the location, and the directions of neighboring vehicles but also the big data such as video of surrounding environments and three-dimensional (3D) high-resolution maps. The transportation control system can use these applications for congestion avoidance, control performance improvement [2], overall traffic efficiency improvement [3], and cyberattack mitigation [4].

In order to provide the reliable and low latency for the V2X services, efforts have been made in recent years to develop V2X communications using IEEE 802.11p [5] and ITS-G5 [6]. Cellular vehicle-to-everything (C-V2X) communication is now regarded as another promising and feasible solution for the fifth-generation mobile networks- (5G-) enabled vehicular communications [7]. C-V2X will allow vehicles to communicate wirelessly with each other, with traffic signs, and with other roadside infrastructures by using the same 5G networks coming to mobile phones.

In [8], the authors propose an architecture that incorporates V2V communications into C-V2X and IEEE 802.11p-based the vehicular ad hoc networks (VANETs). For the frequency bands, 5.9 GHz band has been standardized in the IEEE 802.11p, while ITS-G5 is operating at 5 GHz frequency band. C-V2X will operate on the cellular networks using the same frequency bands as 5G new radio (NR). Frequency band for 5G NR [9] is being separated into two different ranges, including the sub-6 GHz frequency band [10] and millimeter wave (mmWave) frequency band [11]. The very high 5G frequency bands at mmWave, such as 24.25-27.5 GHz schemed in Europe, 24.25-27.5 GHz and 37-43.5 GHz schemed in China, 27.5-28.35 GHz and 37-40 GHz schemed in the United States, will allow the deployment of hotspots providing very high throughput thanks to the large available bandwidth for operators. On the other hand, the sub-6 GHz spectrum is less complicated in the development of infrastructure, deployment, and future network enhancements. Thus, it can be quickly cleared for the early deployment of 5G cellular networks across the globe. Europe has awarded the trial licenses at 3.4-3.8 GHz band [12]. China is ongoing at 2.5-2.6 GHz, 3.4-3.6 GHz, and 4.8-4.9 GHz frequency bands [13], while Korea is planning at 3.4-3.7 GHz. The United States schemes the frequency bands of 3.1-3.55 GHz and 3.7-4.2 GHz. Overall, the frequency from 2.5 GHz to 5.9 GHz is the main sub-6 GHz frequency band for V2X communications. Therefore, it is necessary to thoroughly investigate the V2X channel characteristics at this frequency band in different scenarios.

In the literature, the sub-6 GHz vehicular communication channels for 5G are characterized by academia and industry. Channel measurement is regarded as a valid approach to describe realistic propagation information. Many measurements have been taken in vehicular communications to characterize radio channel [14]. In vehicle communications, measurements are even more challenging due to high mobility scenarios and more dynamic network conditions [15]. The authors of [16] investigate channels under the conditions from Line-of-Sight (LoS) to non-Line-of-Sight (NLoS) in terms of delay spread, Doppler spread, and the RMS delay spreads at 5.9 GHz. The author of [17] present thorough characterizations for intracar propagation based on the practical measurement on-board an HSR at 2.4 and 5.8 GHz. By considering the traffic flows and the velocity of the vehicles, the wireless communications at 2.48 GHz under the NLoS condition are compared between the measurements and proposed time-variant temporal correlation function (TCF) model in [18]. The cross-polarized channel measurements are conducted in a small-cell street canyon scenario at 2.6 GHz [19]. It is found that the polarization does not influence the angles of arrival. In [20], channel measurements in an urban scenario are performed at 2.6 GHz using a virtual uniform linear array (ULA). In [21], the mobility measurements are conducted in an urban macrocellular (UMa) scenario to analyze the path loss at 2.54 GHz, 3.5 GHz, 4.9 GHz, and 5.4 GHz, respectively. Path loss, Ricean *K*-factor, and angular power spectrum are analyzed. The path loss of the measurements in an overpass scenario is fitted by two-ray model at 5 GHz [22]. The distributions of time-varying delay spread and Doppler spread follow a bimodal Gaussian mixture distribution in the street cross scenario at 5.5 GHz [23]. The authors of [24] survey the propagation characteristics at sub-6 GHz and mmWave bands, in which the preferred bands for initial deployment are 3.3-4.2 GHz and 26/28 GHz for 5G communications. The authors of [25] summarize the advanced channel measurements for vehicular communications at sub-6 GHz frequency band.

Channel models can be classified as stochastic and deterministic ones. The geometry-based stochastic channel models (GBSMs) with wide-sense stationary (WSS) assumption for vehicular channels have been widely accepted in the past studies [26, 27]. In [28], the GBSM combined with a two-ray model is proposed for nonisotropic multiple-input multiple-output (MIMO) Ricean fading channels in regular shaped environments and is validated for V2V channel at 5.9 GHz. Moreover, several measurements show that the WSS assumption validates only in a short distance interval and time interval [29]. For the nonstationary vehicular channel modeling, most works focus on the surrounding scatterers, e.g., vehicles, pedestrians [22], and traffic signs [30]. Deterministic channel models, such as ray-tracing (RT), can provide accurate channel information in propagation scenarios. The LoS, reflected, scattered, diffracted, and penetrated multipaths can be traced as rays, which contain the amplitude, angle, and delay information. In [31], the authors integrate the radar cross sections of the small-scale structures (e.g., lampposts and traffic signs) into RT simulator and conduct extensive RT simulations for V2V channel in urban and open space environments at 5 GHz. In [32], the authors propose that RT can be utilized to detect hidden obstacles in an external environment of a vehicle with the help of a light detection and ranging (LIDAR) sensor. In [33], the authors compare the RT simulations against V2V channel measurements using a channel sounder in an urban scenario at 5.9 GHz. The received power, delay spreads, and Doppler spreads are characterized in LoS and NLoS conditions, respectively.

Nevertheless, a comprehensive characterization of V2I channel based on cellular networks at 3.5 GHz frequency band is rarely found. Due to the limits of measurement equipments, propagation scenarios, and traveling speeds of the vehicles, a tendency of vehicular channel characterization is to combine the RT simulations. Thus, in this paper, we characterize the V2I channel at 3.5 GHz based on channel measurements and simulations with the following contributions:

(i) Dynamic channel measurements are performed in a suburban scenario at 3.5 GHz frequency with the bandwidth of 100 MHz, because 3.5 GHz is the common spectrum band in Europe [12], China [13], and other countries of the world for 5G. The transmitter (Tx) is fixed, while the moving receiver (Rx) is carried by a vehicle during the measurements. Double-cone omnidirectional antennas for both Tx and Rx are utilized in the measurements. The power delay profiles (PDPs), path loss (PL), shadow fading (SF), root-mean-square (RMS) delay spread (DS), and the coherence bandwidth are analyzed based on the measured results

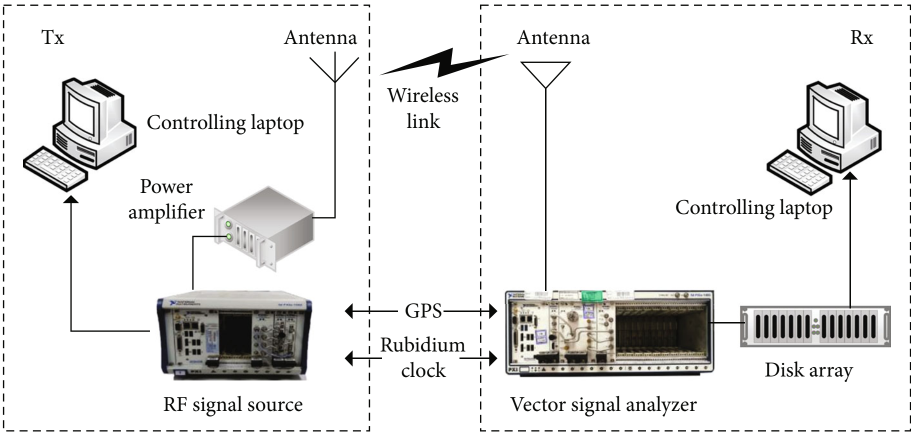

Figure 1: Main structure of measurement system.

Figure 2: Satellite image of the measurement environment and trajectories of moving Rx.

(ii) We reconstruct the suburban scenario and conduct the simulations utilizing the measurement-validated RT simulator with the same configurations as the measurement. The RT simulations breakthrough the limits of the measurement data and expand the measured two-dimensional (2D) channel into a 3D channel. The electromagnetic (EM) properties of relevant materials are calibrated. Then, the channel is characterized more comprehensively with the aid of Ricean *K*-factor (KF), angular spreads, and cross-polarization ratio (XPR). Combined with the channel parameters extracted from measurements, the cross-correlations of the abovementioned parameters are listed, and the autocorrelation of each parameter itself is calculated as well. The provided key parameters of this paper help to understand the V2I channel characteristics and to support the link-level and system-level design. These will enable the C-V2X communications for 5G

The remainder of this paper is organized as follows. The measurement systems and campaigns for the V2I channel are detailed in Section 2. The analysis of the measurement results is described in Section 3. In Section 4, the RT simulations are conducted in the reconstructed measurement scenario. Finally, the conclusions are drawn in Section 5.

2. Channel Measurement Campaign

In order to measure the V2I channel, a dynamic frequency domain channel sounding method is applied in a suburban scenario. As shown in Figure 1, this measurement system is supported by a controlling laptop, a radio frequency (RF) signal source by NI PXIe-5673E module, a power amplifier, and an antenna at the Tx side. At the Rx side, it is composed of a controlling laptop, a wideband vector signal analyzer (VSA) by NI PXIe-5668 module, a disk array, and an antenna. The XHTF3311 global positioning system (GPS) and a rubidium clock are utilized to ensure the synchronization of the signal for Tx and Rx during the measurements. The carrier frequency is 3.5 GHz with a bandwidth of 100 MHz, and the number of frequency points is 821. The transmitting power is 40.77 dBm by the power amplifier. The transmit signal is a Zadoff-Chu (ZC) sequence and can provide an almost constant magnitude in the frequency domain [34].

The measurement campaigns are conducted in Haidian District, Beijing, China. We select the measurement area far from the main road of the city and only conduct the measurements in the evening so that by-passing traffics and pedestrians do not affect the measurements. We measure the LoS scenario, which exists mostly in V2I channels. As shown in Figures 2 and 3, the fixed Tx, with a height of 2.55 m, is at the intersection of the two roads. In the measurements, the Tx transmits signal sequences continuously. In order to emulate a typical vehicular environment, the two crossroads are selected in the measurements. The Rx is carried by a vehicle with a height of 1.88 m (as shown in Figure 3) forward or reversely following the track of the red arrows. Route 1 from north to south (approximately 210 m) represents the vehicle moving towards the fixed Tx, while Route 2 from west to east (approximately 340 m) represents the vehicle moving away from the Tx. Either Tx or Rx is a double-cone omnidirectional antenna with 0 dBi gain. The 3D radiation patterns and the 2D radiation patterns in the horizontal plane (H-

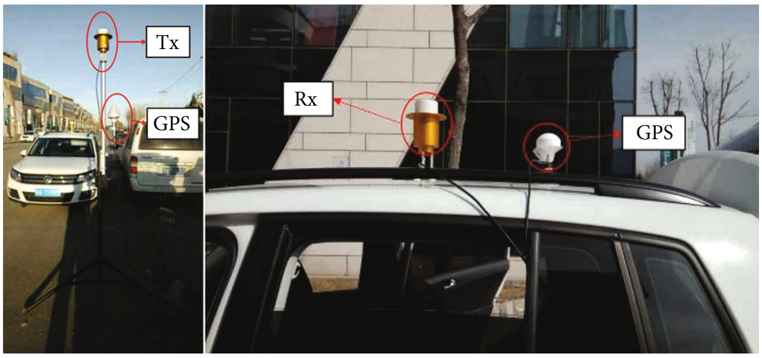

Figure 3: Locations of Tx and Rx.

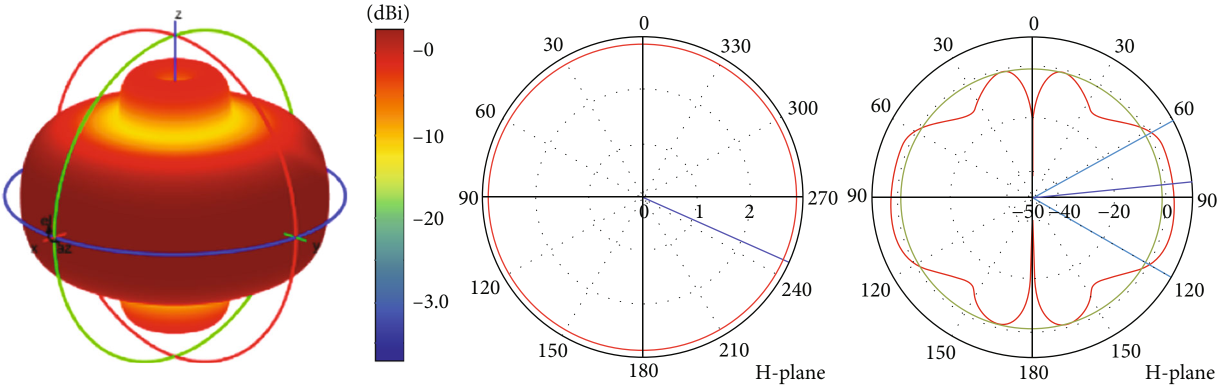

Figure 4: Radiation pattern of the double-cone omnidirectional antenna.

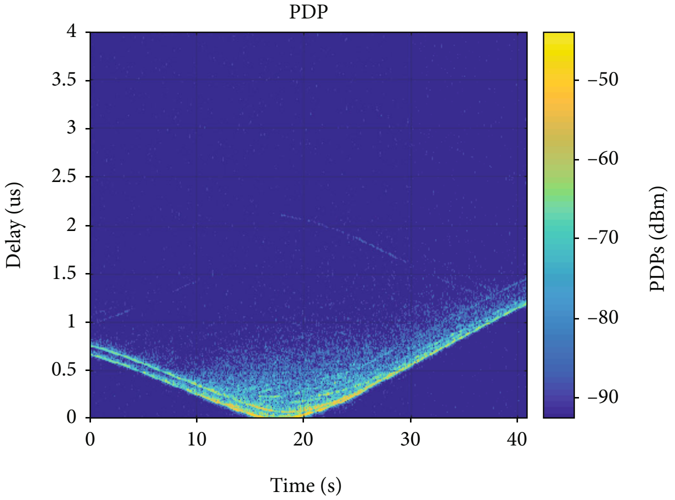

Figure 5: Time-varying PDP.

plane) and elevation plane (E-plane) of utilized antennas are shown in Figure 4.

3. Analysis of Measurement Results

In this section, the measured data are preprocessed in the frequency domain and time domain. The channel characteristics, including PDP, path loss, shadow fading, RMS delay spread, and coherence bandwidth, are calculated and analyzed for the V2I channel as follows.

3.1. Preprocessing. The received signal in the frequency domain can be expressed as follows [34]:

$$Y(d,f) = X(f)H_{Tx}(f)H(d,f)H_{Rx}(f), \tag{1}$$

Table 1: Measured path loss of V2I channel at 3.5 GHz.

Route 1			Route 2		
PL(d_0)	n	σ_{SF}	PL(d_0)	n	σ_{SF}
12.15	2.60	4.91	26.11	1.66	2.19

where $X(f)$ and $Y(d,f)$ are the transmitted and received signals, respectively. d is the distance between Tx and Rx, and f is the operating frequency. $H_{Tx}(f)$ and $H_{Rx}(f)$ are the transfer functions of the Tx and Rx equipment, such as antennas, VSA, and cables, while $H(d,f)$ is the transfer function of the wireless channel. In order to remove the influence of the transceivers, the reference signal measurements with the same setting as in the channel measurements are conducted in an anechoic chamber. The reference received signal can be expressed as follows:

$$Y_{\mathrm{ref}}(f) = X(f)H_{Tx}(f)H_{\mathrm{ref}}(f)H_{Rx}(f), \tag{2}$$

where $H_{\mathrm{ref}}(f)$ is the free space transfer function.

Thus, the channel transfer function (CTF) can be calculated as follows:

$$H(d,f) = \frac{Y(d,f)}{Y_{\mathrm{ref}}(f)}H_{\mathrm{ref}}(f). \tag{3}$$

Then, the channel impulse response (CIR) $h(\tau)$ can be calculated by the inverse Fourier transform:

$$h(\tau) = \mathrm{IFFT}\left(H(f), N_f\right), \tag{4}$$

where τ is the time delay of the received signal and N_f is the effective number of the measured frequency points. A Hann window is used to suppress side lobes, and the sliding window is with the size of 20 wavelengths. A total of 4080 effective CIRs are extracted for the entire travel trajectory.

In addition, at the largest distance between Tx and Rx, the lowest average signal-to-noise-ratio (SNR) is about 20 dB, and at most of the measurement locations, the SNR is over 25 dB. Hence, the accurate estimation of channel parameters is possible in the following part.

3.2. Power Delay Profile. The signal power on each multipath against their respective propagation delay is defined by the PDP, which is defined as:

$$P(t,\tau) = |h(t,\tau)|^2. \tag{5}$$

A time-varying PDP of the measurement is shown in Figure 5. The calculated optimal threshold after filtering noise is -95.69 dBm, which is 6 dB higher than the mean value of the noise power and effectively separates the signal from noise. The dynamic range is larger than 40 dB. Then, the local maximums as the "peaks" higher than the noise threshold are identified as the "paths." It can be seen clearly that in the propagation environment, there are always two energy-intensive paths. One is the LoS path, and the other is the strongly reflected path from the ground. Besides, there are rich multipaths in the whole scenario.

Table 2: RMS delay spread and coherence bandwidth.

RMS delay spread (ns)		Coherence bandwidth (MHz)	
μ_{DS}	σ_{DS}	μ_{B_c}	σ_{B_c}
670.34	355.69	15.83	11.10

3.3. Path Loss Exponent and Shadow Fading. The local wideband path gain PG(d) can be calculated directly from the measured CTFs in the frequency domain as follows:

$$\mathrm{PG}(d) = \frac{1}{N_f}\left(\sum_{l=1}^{N_f}|H(d,f_l)|^2\right), \tag{6}$$

where f_l is the sampling frequency and $N_f = 821$ is the number of the measured frequency points. As can be seen from Figure 2, the moving track of Route 1 is Rx towards the fixed Tx, while the moving track of Route 2 is Rx away from the fixed Tx. The environments and the length of these two roads are not similar. In Route 1, there are buildings along the two sides of the road, while only one side of Route 2 has buildings, and the other side is a fence with advertisements. Thus, two routes should be separated to analyze. To remove the effect of small scale fading, in this paper, we use a sliding window with the size of 20 wavelengths for averaging.

The log-distance path loss model is to fit the opposite number of measured path gain. The change of the path loss, along with the distance, is depicted by the path loss exponent. This exponent and shadow fading are extracted from the measured results by using the following expression [35]:

$$\mathrm{PL}(d) = \bar{\mathrm{PL}}(d_0) + 10n\left(\log_{10}\frac{d}{d_0}\right) + X_\sigma, \tag{7}$$

where PL(d) is the path loss and d is the distance between the Tx and Rx in m. d_0 is the reference distance; we choose the measured PL at $d_0 = 10$ m as a reference in our study. PL(d_0) is the media path loss at d_0, and n is the path loss exponent. By using the least-square criterion, the path loss exponent n can be obtained. X_σ is the shadow fading, which can be expressed as a Gaussian variable with zero mean value and a standard deviation of σ_{SF}. The path loss exponent and the shadow fading standard deviations based on the measurements are summarized in Table 1. The fact of higher path loss exponent n and higher σ_{SF} for Route 1 indicates a more complicated environmental condition of the Route 1. There are a large number of trees, two rows of iron fences, and concrete walls on the side of Route 1, which cause the scattering during the wireless propagation.

3.4. RMS Delay Spread and Coherence Bandwidth. The RMS delay spread is one of the key parameters for a multipath channel. It is defined in [36], namely, the square root of the

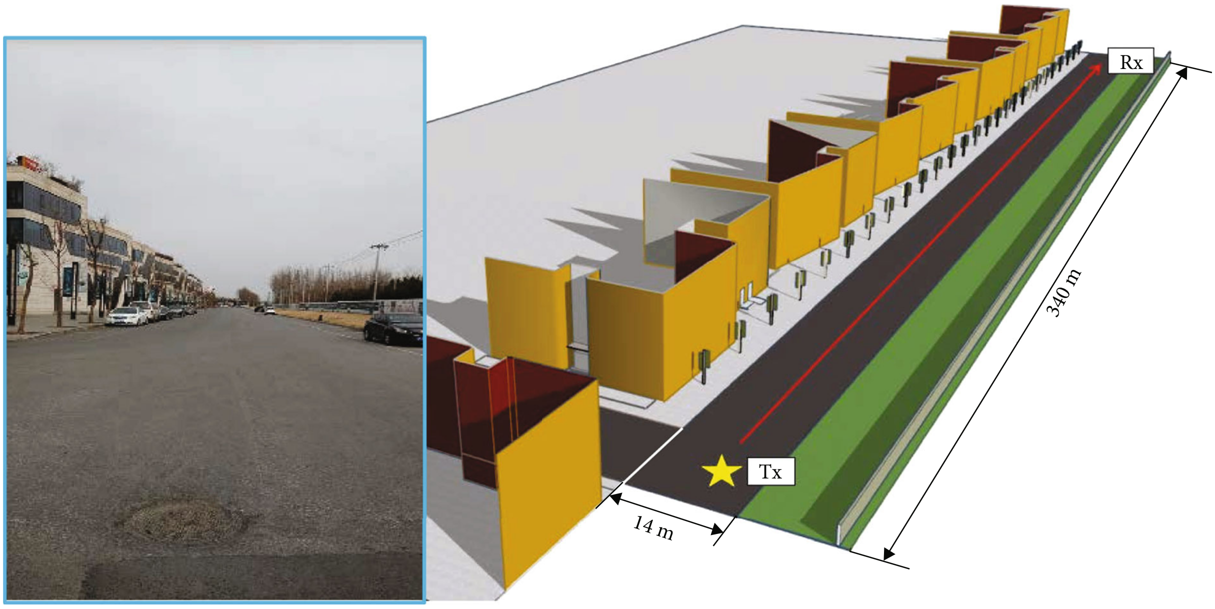

Figure 6: 3D model of the reconstructed suburban scenario.

Table 3: Simulation configurations.

Parameter	Value
Center frequency	3.5 GHz
Bandwidth	100 MHz
Frequency points	821
Tx height	2.55 m
Rx height	1.88 m
Polarization	VV, HH, VH, and HV
Tx power	40.77 dBm
Propagation mechanism	LOS + up to 3rd order of reflection + scattering + diffraction

second central moment of the PDP as follows:

$$\sigma_\tau = \sqrt{\frac{\sum_{n=1}^{N} {\tau_n}^2 \cdot P_n}{\sum_{n=1}^{N} P_n} - \left(\frac{\sum_{n=1}^{N} \tau_n \cdot P_n}{\sum_{n=1}^{N} P_n}\right)^2}, \tag{8}$$

where σ_τ denotes the RMS delay spread and P_n and τ_n denote the power and the excess delay of the n-th multipaths, respectively. The distribution of RMS delay spreads for the whole trajectory is following a Gaussian distribution. The mean value (μ_{DS}) of the measurement routes is 670.34 ns with the standard deviation (σ_{DS}) 355.69 ns. It is in line with the outdoor suburban environment, where the RMS delay spread value is 0.2-2.0 μs. In [23], the RMS delay spreads around 47 ns and 75 ns are measured in urban and tunnel scenario, respectively. However, sometimes, although the LoS component exists in the channel, several significant reflected multipaths and scattered multipaths can still result in a large delay spread, such as in our study.

The inversely proportional relation between RMS delay spread σ_τ and the coherence bandwidth B_c can be expressed:

$$B_c = 1\kappa\sigma_\tau, \tag{9}$$

where κ is a constant that depends on the environment or/and on how B_c is defined. B_c can be defined as the bandwidth at which the complex correlation function has a value of 0.5, 0.9, or even 0.95. For example, $R_H(\Delta f) = 0.5$ means the coherence bandwidth can be specifically denoted as $B_{c,0.5}$ with subscript 0.5 as the threshold [37].

The frequency correlation function of the channel $R_H(\Delta f)$ can be obtained by setting a reasonable threshold [38]:

$$R_H(\Delta f) = \int_{-\infty}^{\infty} P(\tau) e^{-j2\pi\Delta f\tau} d\tau, \tag{10}$$

where $P(\tau)$ is the CIR at a specific time delay τ. The statistical estimation of the mean value μ_{Bc} and the standard deviation σ_{Bc} of coherence bandwidths can be obtained according to the threshold of 0.5 in our study. The values of RMS delay spread and coherence bandwidths are summarized in Table 2. The coherence bandwidth is narrower when using the onmi-directional antennas. It is consistent with the RMS delay spread results and the inverse relation between these two parameters. As happens with the RMS delay spread, the multipath propagation causes the coherence bandwidth.

Moreover, the study on Doppler spectrum of these measurement campaigns has been published in [39]. It can be concluded that the faster the vehicle (Rx) moves, the larger the Doppler spreads. The most significant scatterers during the measurements are trees and billboards, whereas other cars parked on the roadside do not significantly contribute to the multipath propagation.

4. RT Simulation for V2I Channels at 3.5 GHZ

In order to physically interpret the measurement results, a self-developed dynamic RT simulator of Beijing Jiaotong University is used in this study. Supported by high-performance computing (HPC), this RT simulator is now furnished to an HPC cloud-based platform (CloudRT), which contains 1600 CPUs and 10 GPUs. Parallel processing can be implemented by a compute node or monitored by a management node. The first premise of accurate ray-tracing simulation is a thorough and factual description of the scenarios. The finer the scenarios modeled, the more accurate the corresponding prediction is. Also, simulation time is proportional to the accuracy. The simulation time for a single snapshot in this article is about 10 seconds, and the total simulation time depends on the number of nodes selected for parallel computing. More details of this platform can be found in [40] and the website http://raytracer.cloud.

As shown in Figure 6, the 3D model of the suburban scenario is reconstructed through SketchUp [41] and OpenStreet Map [42]. The asphalt road of Route 2 is with a width of 14 m and with a length of 340 m. The height of the office buildings on the one side is about 15-20 m. In order to simulate the channel for 100 MHz bandwidth, we use the subband RT approach. The CIR for one snapshot is generated by a number of subbands at multiple center frequency points [43]. Based on the measurement configurations in the same scenario, 821 frequency points are determined. Since the relevant materials are not frequency sensitive, the constant EM properties of them are used for all subbands at 3.5 GHz. The LoS ray, reflected rays (up to third order), scattered rays, and diffracted rays are traced in the simulations for the trade-off between simulation accuracy and computational complexity. The directive scattering model [44] and the uniform theory of diffraction (UTD) model [45] are used in the simulations. In order to get the pure propagation channel without the influence of certain antenna pattern, the antenna of Tx or Rx is omnidirectional antenna, which is in line with the measurements. In addition, in order to get the fully polarimetric information of the channel, the antennas of Tx and Rx are with four cases of polarization: vertical-vertical (VV) polarization, vertical-horizontal (VH) polarization, horizontal-vertical (HV) polarization, and horizontal-

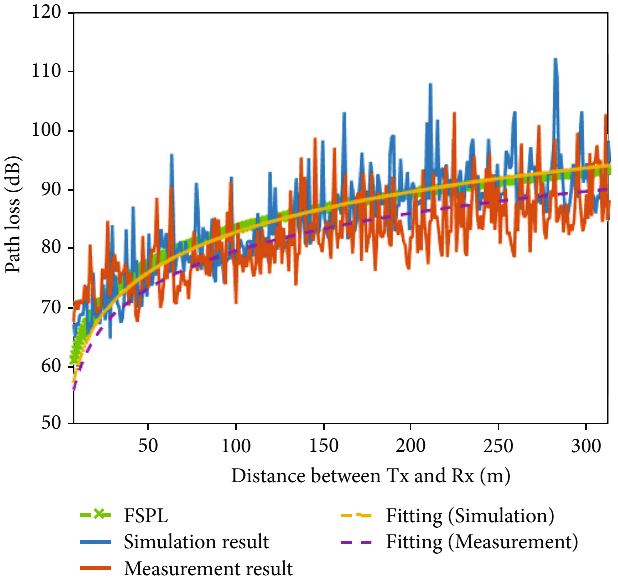

Figure 7: Path loss (measurement vs. validated and calibrated simulation).

Table 4: Material EM properties before and after calibration.

Material name	Before calibration		After calibration	
	$\varepsilon 0r$	$\varepsilon 00_r$	$\varepsilon 0r$	$\varepsilon 00_r$
Concrete	1.06	0.65	5.60	0.05
Tempered glass	9.99	0.43	6.27	0.33
Brick	2.00	0.25	6.09	0.08
Vegetation	29.12	0.278	10.00	0.15
Stainless steel	1.00	1*E*07	1.00	1*E*07
Granite	1.25	1.79	4.25	0.78
Canvas2.94	2.94	0.04	2.61	0.45

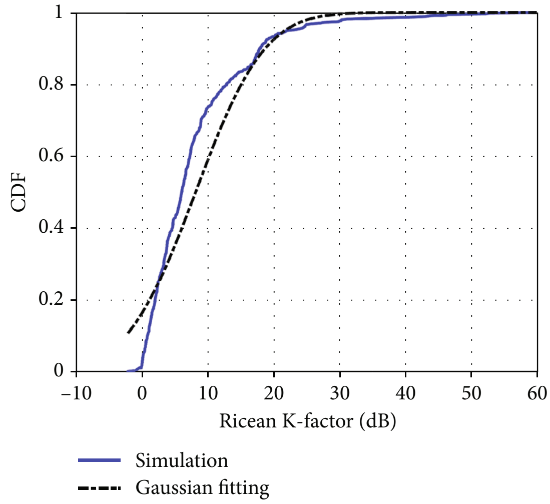

Figure 8: Ricean *K*-factor.

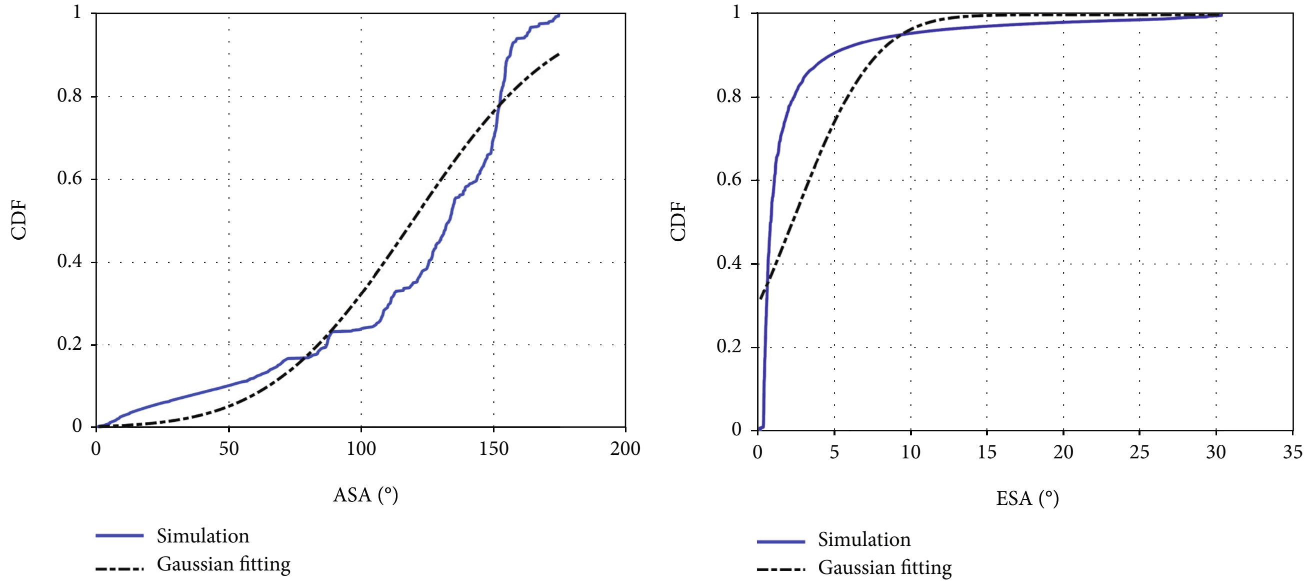

(a) ASA

(b) ESA

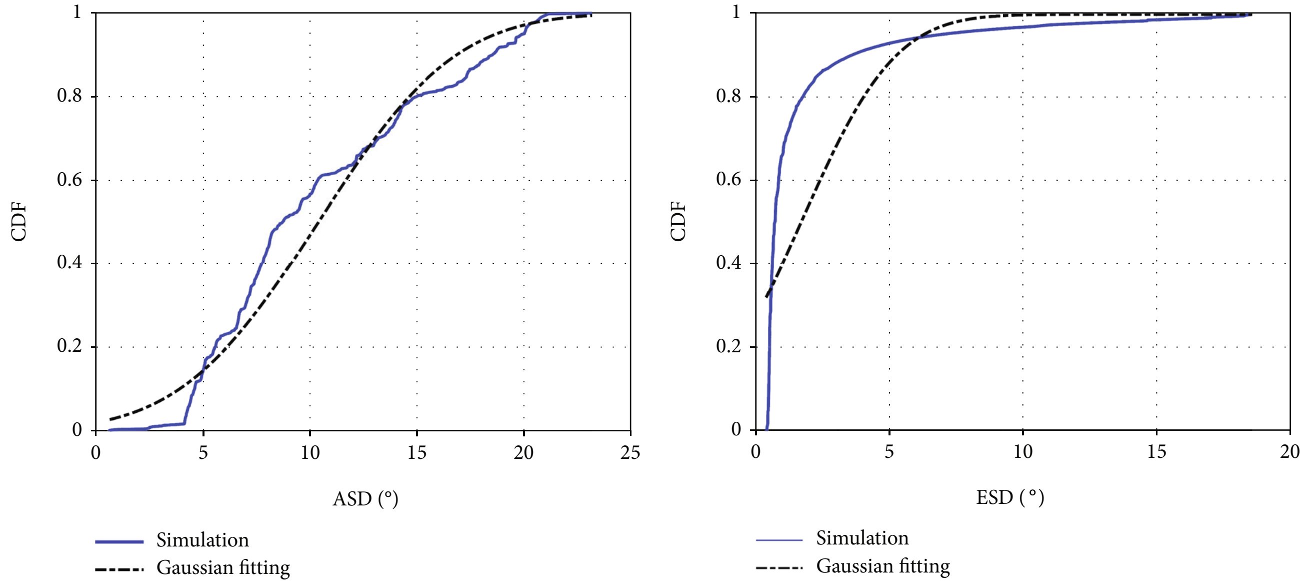

(c) ASD

(d) ESD

Figure 9: Angular spreads.

horizontal (HH) polarization in the extensive RT simulations. Table 3 summarizes the simulation configurations.

4.1. Validation and Calibration of RT Simulator. Several snapshots are stochastically chosen to validate the geometry and calibration of the EM properties of the suburban scenario, where the validation and calibration processes are according to our previous work [46]. Figure 7, as an example, shows the comparison of path loss between the measurement and the validated and calibrated RT simulation. The antenna influence can be neglected with the omnidirectional antennas both at Tx and Rx sides. Compared with the measurement results, the difference of path loss exponent n between simulation and measurement is 0.12, with the relative error 6.4%. The difference between the shadow fading is 0.29 dB, and the relative error is 5.6%, which proves the accuracy of the RT simulator in channel simulation. The calibrated EM properties are summarized in Table 4, which will be used in the following extensive simulations.

4.2. Channel Characterization Based on Extensive RT Simulations. The extensive RT simulations are done for more comprehensive channel characterization. Route 2 selected as an example, the key parameters can be supplemented to fully describe for the V2I channel, in terms of the Ricean K-factor, XPR, and four angular spreads (namely, azimuth angular spread of arrival (ASA), azimuth angular spread of departure (ASD), elevation angular spread of arrival (ESA), and elevation spread of departure (ESD)). Combined with the channel parameters extracted from the measurements, the cross-

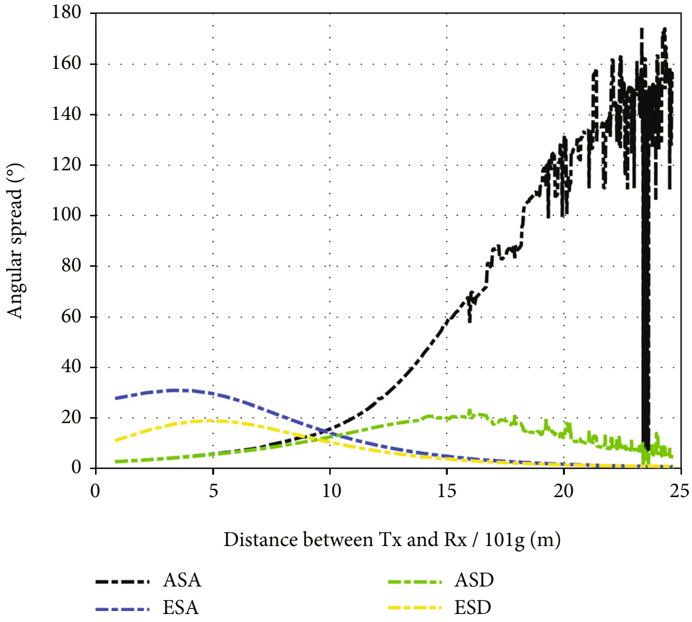

FIGURE 10: Angular domain parameters changes with distance.

correlations of the abovementioned parameters are listed, and the autocorrelation of each parameter itself is calculated as well.

4.2.1. Ricean K-Factor. The Ricean *K*-factor is defined as the ratio of the signal power of the LoS path to the signal power of other multipath components, which can be expressed as:

$$\mathrm{KF} = \frac{P_{LoS}}{\sum P(i) - P_{LoS}}, \tag{11}$$

where $P(i)$ is the energy of all the paths of the signal during transmission and P_{LoS} is the energy of the LoS path. As shown in Figure 8, most values of the *K*-factor are larger than 0 dB. When the probability is 0.5, the corresponding value of KF is 5.98 dB; when it reaches 0.9, the value is 18.16 dB. Such high values indicate that the LoS component plays the leading role in the propagation scenario, while the multipaths reflected from the surfaces of the buildings and the ground are relatively weak.

4.2.2. Angular Spreads. The angular spread is the distribution of the angle of arrival/departure of each multipath in 3D environments for the Tx and Rx, respectively. Each multipath is assigned an azimuth angle in the horizontal plane and an elevation angle in the vertical plane. Hence, four values of angular spreads can be calculated as follows:

$$\sigma_{\mathrm{AS}} = \sqrt{\frac{\sum_{n=1}^{N} \left(\theta_{n,\mu}\right)^2 \cdot P_n}{\sum_{n=1}^{N} P_n}}, \tag{12}$$

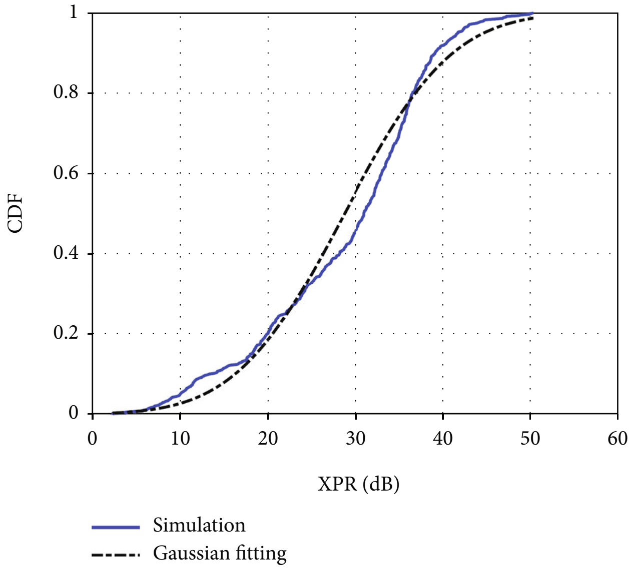

FIGURE 11: XPR.

TABLE 5: Decorrelation length of key parameters.

λ (m)	SF	KF	DS	ASD	ASA	ESD	ESA
Value	1.2	10.5	2.2	9.0	8.0	7.5	9.5

where σ_{AS} denotes the angular spread (AS), P_n denotes the power of the n-th multipath, and $\theta_{n,\mu}$ is defined by:

$$\theta_{n,\mu} = \bmod\left(\theta_n - \mu_\theta + \pi, 2\pi\right) - \pi, \tag{13}$$

where θ_n is the azimuth angle of arrival (AoA)/azimuth angle of departure (AoD)/elevation angle of arrival

(EoA)/elevation angle of departure (EoD) of the n-th ray. μ_θ is:

$$\mu_\theta = \frac{\sum_{n=1}^{N} \theta_n \cdot P_n}{\sum_{n=1}^{N} P_n}. \tag{14}$$

Figure 9 shows the CDFs of the four angular spreads, including ASA, ESA, ASD, and ESD, respectively. Most elevation angular spreads are below 10°, which is much smaller than azimuth angular spreads in the horizontal plane. In general, the scattering effect in the horizontal direction is stronger than it in the vertical direction, because of the multipath components reflected from the infrastructures along the roadside. We further analyze the variation of the angular spreads during the vehicle moving trajectory, as shown in Figure 10. The values of ESA and ESD are more significant than those of ASA and ASD when the distance between Tx and Rx is within 10 m. This observation implies that multipaths reflected from the ground in the vertical direction are stronger than those in the horizontal direction at the beginning. As the distance increases, the values of ASA and ASD are larger than those of ESA and ESD. Concerning the ASA, it increases sharply to 173° due to energetic scattered paths from the infrastructures far away from the Tx but close to Rx.

4.2.3. XPR. The XPR is to describe the variety of the polarization for the multipath components and is calculated by its definition as follows:

$$\mathrm{XPR} = 10 \log_{10}\left(\frac{P_{\mathrm{co}}}{P_{\mathrm{cross}}}\right), \tag{15}$$

where P_{co} is copolarization defined by the received power when Tx and Rx antennas polarize in the same manner. Conversely, P_{cross} is the power received in vertical (horizontal) polarization and transmitted in horizontal (vertical) polarization. As shown in Figure 11, the high values imply little depolarization in such a suburban scenario. These values are much larger than the higher frequency band in similar scenarios, such as at 28 GHz [47] and at THz band [48]. Generally speaking, the linear polarization of the antennas is sufficient in such a scenario.

4.2.4. Autocorrelation and Decorrelation Distance. The autocorrelation function of a parameter X is to describe how fast a certain variable changes with the distance interval Δd (or time delay τ), which can be calculated as follows:

$$R(\Delta d) = \frac{E[(X_d - \mu)(X_{d+\Delta d} - \mu)]}{\sigma_X^2}, \tag{16}$$

where E is the expected value operator. Correspondingly, the decorrelation distance λ in (m) is expressed as:

$$\lambda = \underset{\Delta d > 0}{\operatorname{argmax}}(|R(\Delta d)| < T), \tag{17}$$

where T is the threshold.

Table 6: Cross-correlation of the channel parameters.

Parameter	DS	KF	SF	ASD	ASA	ESD	ESA
DS	1	0.25	-0.07	0.12	-0.02	-0.09	-0.11
KF		1	-0.04	-0.61	-0.59	-0.39	-0.38
SF			1	0.01	0.02	-0.02	-0.02
ASD				1	-0.58	-0.22	0.12
ASA					1	-0.76	-0.74
ESD						1	0.99
ESA							1

Table 7: Key parameters of V2I channel at 3.5 GHz.

	DS (ns)	B_c (MHz)	KF (dB)	ASA (°)	ESA (°)	ASD (°)	ESD (°)	XPR (dB)
μ	670.34	15.83	6.73	117.4	2.18	10.47	1.70	28.64
σ	355.69	11.10	8.23	1.63	0.63	0.70	0.44	9.69
λ (m)	2.2	—	10.5	9.0	8.0	7.5	9.5	—

The larger the threshold is set, the stricter the correlation requirements are, and the smaller the decorrelation distance is. The threshold is generally a practical value. The common value of 0.9 is set in our study. Table 5 summarizes the decorrelation distance of each parameter. It can be preconcluded that the shadow fading is not self-correlated. The KF and DS are highly self-related. The value of the decorrelation distances of the parameters mentioned above is in line with the values provided by 3GPP 38.901 [49].

4.2.5. Cross-Correlation. We consider a wideband V2I channel, study the key parameters of the channels across 100 MHz at 3.5 GHz frequency band, and try to capture the channel correlation across different parameters. The cross-correlation coefficient of the two variables is a measure of their linear dependence. If each variable has N scalar observations, then the Pearson cross-correlation coefficient is defined as:

$$R_{A,B} = \frac{1}{N-1} \sum_{i=1}^{N} \left(\frac{A_i - \mu_A}{\sigma_A}\right)\left(\frac{B_i - \mu_B}{\sigma_B}\right), \tag{18}$$

where A_i and B_i represent two different aforementioned channel parameters and μ and σ denote the mean value and the standard deviation of corresponding parameters, respectively.

Combined with the measurements and simulation results, the cross-correlations of the key parameters are summarized in Table 6. It can be found that shadow fading is not cross-correlated with other key parameters since the correlations of it with other key parameters are approximately equal to 0. Remarkably, KF is negatively correlated to the angular spreads, since with a large value of KF, a significant component comes from a single direction leading to smaller angular spreads. In the angular domain, the parameters show relatively strong correlations between each other. If the variables of interest are highly correlated, it can be used to make accurate predictions.

4.2.6. Summary of the Channel Parameters by Measurements and Simulations. The V2I channel is comprehensively characterized based on the measurements and simulation together. The group of channel parameters can be summarized in Table 7. The validation results of path loss indicate that RT can practically reflect the target scenarios. Besides, the RT simulations can break the limits of the measurement data. Reliable channel information can be obtained with similar materials. Moreover, other important channel information, such as angles, which are not captured from the measurements easily, can be given by RT simulations.

5. Conclusion

In this paper, we comprehensively characterize the V2I channel through the combination of the measurements and simulations in a suburban scenario at 3.5 GHz band for 5G communications. To begin with, the channel measurements are conducted in a typical vehicular scenario. The track of moving vehicle is separated into two routes, where the environment of Route 1 is more complicated than Route 2. The time-varying PDP, path loss, RMS delay spread, and the coherence bandwidth are extracted from the channel measurements. From the time-variant power delay profiles, it can be clearly seen that two significant paths always exist during the measurements. It indicates that the LoS vehicular channel measurement generally follows the classic two-ray models. One is the LoS path, and the other is the reflected path from the ground. The path loss exponent n and the σ_{SF} are extracted to describe the path loss and shadow fading, respectively. Because of the more complicated environment of Route 1, the values of n and σ_{SF} are larger than these of Route 2. The coherence bandwidth is to follow the inversely proportional relation to RMS delay spreads. As the threshold is set 0.5, the coherence bandwidth then can be calculated and analyzed.

Moreover, the RT simulations are conducted in order to supply other key parameters. The high-performance self-developed RT simulator of Beijing Jiaotong University is utilized in our study. The RT simulations breakthrough the limits of the measurement data and expand the measured 2D channel into a 3D channel. After validated and calibrated by the measured PDPs and compared with the path loss, the RT simulator is utilized to do extensive simulations in a reconstructed suburban scenario. The large value of Ricean K-factor implies the LoS leading a significant role in the propagation. Four cases of the vertical/horizontal polarization of antennas for Tx and Rx are schemed to characterize the fully polarimetric information of the channel. The analysis of the XPR shows little depolarization in such a LoS condition. The angular spreads (ASA, ESA, ASD, and ESD) are analyzed. When the distance between Tx and Rx is within 10 m, the multipaths reflected from the ground are stronger than the multipaths reflected/scattered from the infrastructures, iron fences, and tress. As the distance increases, the azimuth angular spreads become larger than elevation angular spreads. Moreover, the decorrelation distance of each parameter and the cross-correlations of the abovementioned parameters are supplied. SF is neither self-correlated nor cross-correlated with other channel parameters. KF is negatively correlated to the four angular spreads, since a significant component coming from a single direction leads to a large value of KF but small angular spreads.

In summary, the group of channel parameters is thoroughly analyzed, and the V2I channel is comprehensively characterized based on the measurements and simulations. This study on channel characteristics at 3.5 GHz can be applied to the link-level and system-level design for the C-V2X communications of 5G.

Data Availability

The raw data required to reproduce these findings cannot be shared at this time as the data also forms part of an ongoing study.

Conflicts of Interest

The authors declare that they have no conflicts of interest.

Acknowledgments

This work is supported by the Key-Area Research and Development Program of Guangdong Province, China (2019B010157001), the State Key Laboratory of Rail Traffic Control and Safety (Contract No. RCS2020ZZ005), and the NSFC under Grants 61771036, 61911530260, 61901029, and 61725101.

References

[1] Y. Ji, W. Fan, M. G. Nilsson et al., “Virtual drive testing over-the-air for vehicular communications,” *IEEE Transactions on Vehicular Technology*, vol. 69, no. 2, pp. 1203–1213, 2020.

[2] L. Zhu, F. R. Yu, B. Ning, and T. Tang, “Cross-layer handoff design in mimo-enabled wlans for communication-based train control (CBTC) systems,” *IEEE Journal on Selected Areas in Communications*, vol. 30, no. 4, pp. 719–728, 2012.

[3] K. M. S. Huq, S. A. Busari, J. Rodriguez, V. Frascolla, W. Bazzi, and D. C. Sicker, “Terahertz-enabled wireless system for beyond-5G ultra-fast networks: a brief survey,” *IEEE Network*, vol. 33, no. 4, pp. 89–95, 2019.

[4] L. Zhu, Y. Li, F. R. Yu, B. Ning, T. Tang, and X. Wang, “Cross-layer defense methods for jamming-resistant CBTC systems,” *IEEE Transactions on Intelligent Transportation Systems*, pp. 1–13, 2020.

[5] D. Jiang and L. Delgrossi, “IEEE 802.11p: towards an international standard for wireless access in vehicular environments,” in *VTC Spring 2008 - IEEE Vehicular Technology Conference*, pp. 2036–2040, Singapore, Singapore, May 2008.

[6] T. Etsi, “Intelligent Transport Systems (ITS); European profile standard on the physical and medium access layer of 5 GHz ITS,” *Draft ETSI ES*, vol. 202, no. 663, p. V0, 2009.

[7] L. Zhang, Q. Ni, M. Zhai, J. Moreno, and C. Briso, “An ensemble learning scheme for indoor-outdoor classification based on KPIs of LTE network,” *IEEE Access*, vol. 7, pp. 63057–63065, 2019.

[8] F. Abbas, P. Fan, and Z. Khan, “A novel low-latency V2V resource allocation scheme based on cellular V2X communications,” *IEEE Transactions on Intelligent Transportation Systems*, vol. 20, no. 6, pp. 2185–2197, 2019.

[9] F. Luo, “5G new radio (NR): standard and technology,” *ZTE Communications*, vol. 1, 2017.

[10] “NR; user equipment (UE) radio transmission and reception; part 1: range 1 standalone,” 3GPP TS 38.101-1, Tech. Rep., 2020.

[11] “NR; user equipment (UE) radio transmission and reception; part 2: range 2 standalone,” 3GPP TS 38.101-2, Tech. Rep., 2020.

[12] A. Sgora, “5G spectrum and regulatory policy in Europe: an overview,” in *2018 Global Information Infrastructure and Networking Symposium (GIIS)*, pp. 1–5, Thessaloniki, Greece, October 2018.

[13] “The ministry of industry and information technology publicly sought advice on the use of the 3.3-3.6 GHz and 4.8-5 GHz frequency bands for 5G,” 2016, http://www.soecc.org.cn/show.asp?id=8885.

[14] C. Li, J. Yu, W. Chen, K. Yang, and F. Li, “Shadowing correlation and a novel statistical model for inland river radio channel,” in *ICC 2019 - 2019 IEEE International Conference on Communications (ICC)*, pp. 1–6, Shanghai, China, May 2019.

[15] W. Fan, L. Hentila, F. Zhang, P. Kyosti, and G. F. Pedersen, “Virtual drive testing of adaptive antenna systems in dynamic propagation scenarios for vehicle communications,” *IEEE Access*, vol. 6, pp. 7829–7838, 2018.

[16] J. Yu, W. Chen, F. Li et al., “Channel measurement and modeling of the small-scale fading characteristics for urban inland river environment,” *IEEE Transactions on Wireless Communications*, vol. 19, no. 5, pp. 3376–3389, 2020.

[17] L. Zhang, J. Moreno, and C. Briso, “Experimental characterisation and modelling of intra-car communications inside high-speed trains,” *IET Microwaves, Antennas Propagation*, vol. 13, no. 8, pp. 1060–1064, 2019.

[18] Q. Zhu, W. Li, C.-X. Wang et al., “Temporal correlations for a non-stationary vehicle-to-vehicle channel model allowing velocity variations,” *IEEE Communications Letters*, vol. 23, no. 7, pp. 1280–1284, 2019.

[19] R. Zhang, L. Cai, Z. Zhong, J. Zhao, and J. Zhou, “Cross-polarized three-dimensional channel measurement and modeling for small-cell street canyon scenario,” *IEEE Transactions on Vehicular Technology*, vol. 67, no. 9, pp. 7969–7983, 2018.

[20] X. Gao, O. Edfors, F. Rusek, and F. Tufvesson, “Massive MIMO performance evaluation based on measured propagation data,” *IEEE Transactions on Wireless Communications*, vol. 14, no. 7, pp. 3899–3911, 2015.

[21] W. Zhang, L. Tian, T. Jiang, A. Huang, J. Zhang, and Y. Zheng, “Analysis on frequency dependence of large scale fading in urban environment,” in *2019 13th European Conference on Antennas and Propagation (EuCAP)*, pp. 1–5, Krakow, Poland, March 2019.

[22] P. Liu, B. Ai, D. W. Matolak, R. Sun, and Y. Li, “5-GHz vehicle-to-vehicle channel characterization for example overpass channels,” *IEEE Transactions on Vehicular Technology*, vol. 65, no. 8, pp. 5862–5873, 2016.

[23] L. Bernado, T. Zemen, F. Tufvesson, A. F. Molisch, and C. F. Mecklenbrauker, “Delay and Doppler spreads of nonstationary vehicular channels for safety-relevant scenarios,” *IEEE Transactions on Vehicular Technology*, vol. 63, no. 1, pp. 82–93, 2014.

[24] M. Shafi, J. Zhang, H. Tataria et al., “Microwave vs. millimeter-wave propagation channels: key differences and impact on 5G cellular systems,” *IEEE Communications Magazine*, vol. 56, no. 12, pp. 14–20, 2018.

[25] X. Cheng, R. Zhang, L. Yang, X. Cheng, R. Zhang, and L. Yang, “Vehicular channel characteristics and modeling,” in *5G-Enabled Vehicular Communications and Networking*, pp. 11–40, Springer, 2019.

[26] X. C. Z. W. Huang and N. Zhang, “An improved non-geometrical stochastic model for non-WSSUS vehicle-to-vehicle channels,” *ZTE Communications*, vol. 17, no. 4, 2019.

[27] L. Zhu, Y. He, F. R. Yu, B. Ning, T. Tang, and N. Zhao, “Communication-based train control system performance optimization using deep reinforcement learning,” *IEEE Transactions on Vehicular Technology*, vol. 66, no. 12, pp. 10705–10717, 2017.

[28] X. Cheng, C.-X. Wang, D. I. Laurenson, S. Salous, and A. V. Vasilakos, “An adaptive geometry-based stochastic model for non-isotropic MIMO mobile-to-mobile channels,” *IEEE Transactions on Wireless Communications*, vol. 8, no. 9, pp. 4824–4835, 2009.

[29] W. Li, Q. Zhu, C.-X. Wang, F. Bai, X. Chen, and D. Xu, “A practical non-stationary channel model for vehicle-to-vehicle MIMO communications,” 2020, https://arxiv.org/abs/2002.00166.

[30] K. Guan, B. Ai, M. L. Nicolas et al., “On the influence of scattering from traffic signs in vehicle- to-x communications,” *IEEE Transactions on Vehicular Technology*, vol. 65, no. 8, pp. 5835–5849, 2016.

[31] K. Guan, D. He, B. Ai et al., “5-GHz obstructed vehicle-to-vehicle channel characterization for internet of intelligent vehicles,” *IEEE Internet of Things Journal*, vol. 6, no. 1, pp. 100–110, 2019.

[32] X. Mei, K. Sakai, and N. Kamata, “Ray tracing for hidden obstacle detection,” 2018, uS Patent 10,078,335.

[33] T. Abbas, J. Nuckelt, T. Kurner, T. Zemen, C. F. Mecklenbrauker, and F. Tufvesson, “Simulation and measurement-based vehicle-to-vehicle channel characterization: accuracy and constraint analysis,” *IEEE Transactions on Antennas and Propagation*, vol. 63, no. 7, pp. 3208–3218, 2015.

[34] R. He, A. F. Molisch, F. Tufvesson, Z. Zhong, B. Ai, and T. Zhang, “Vehicle-to-vehicle propagation models with large vehicle obstructions,” *IEEE Transactions on Intelligent Transportation Systems*, vol. 15, no. 5, pp. 2237–2248, 2014.

[35] K. Guan, B. Ai, Z. Zhong et al., “Measurements and analysis of large-scale fading characteristics in curved subway tunnels at 920 MHz, 2400 MHz, and 5705 MHz,” *IEEE Transactions on Intelligent Transportation Systems*, vol. 16, no. 5, pp. 2393–2405, 2015.

[36] T. Rappaport, *Wireless Communications: Principles and Practice*, Prentice-Hall, Upper Saddle River, NJ, USA, 22nd edition, 2002.

[37] X. Chen, P. Kildal, C. Orlenius, and J. Carlsson, “Channel sounding of loaded reverberation chamber for over-the-air testing of wireless devices: coherence bandwidth versus average mode bandwidth and delay spread,” *IEEE Antennas and Wireless Propagation Letters*, vol. 8, pp. 678–681, 2009.

[38] M. S. Varela and M. G. Sanchez, "RMS delay and coherence bandwidth measurements in indoor radio channels in the UHF band," *IEEE Transactions on Vehicular Technology*, vol. 50, no. 2, pp. 515–525, 2001.

[39] S. Wang, K. Guan, D. He et al., "Doppler shift and coherence time of 5G vehicular channels at 3.5 GHz," in *2018 IEEE International Symposium on Antennas and Propagation & USNC/URSI National Radio Science Meeting*, pp. 2005-2006, Boston, MA, USA, July 2018.

[40] D. He, B. Ai, K. Guan, L. Wang, Z. Zhong, and T. Kurner, "The design and applications of high-performance ray-tracing simulation platform for 5G and beyond wireless communications: a tutorial," *IEEE Communications Surveys Tutorials*, vol. 21, no. 1, pp. 10–27, 2019.

[41] https://www.sketchup.com/.

[42] https://www.openstreetmap.org/.

[43] S. Priebe, *Towards THz Communications: Propagation Studies, Indoor Channel Modelling and Interference Investigations*, Ph.D. Dissertation, Technische Universitat Braunschweig, 2013.

[44] V. Degli-Esposti, F. Fuschini, E. M. Vitucci, and G. Falciasecca, "Measurement and modelling of scattering from buildings," *IEEE Transactions on Antennas and Propagation*, vol. 55, no. 1, pp. 143–153, 2007.

[45] P. Pathak, W. Burnside, and R. Marhefka, "A uniform GTD analysis of the diffraction of electromagnetic waves by a smooth convex surface," *IEEE Transactions on Antennas and Propagation*, vol. 28, no. 5, pp. 631–642, 1980.

[46] D. He, K. Guan, A. Fricke et al., "Stochastic channel modeling for kiosk applications in the terahertz band," *IEEE Transactions on Terahertz Science and Technology*, vol. 7, no. 5, pp. 502–513, 2017.

[47] L. Wang, B. Ai, D. He et al., "Vehicle-to-infrastructure channel characterization in urban environment at 28 GHz," *China Communications*, vol. 16, no. 2, pp. 36–48, 2019.

[48] H. Yi, K. Guan, D. He, B. Ai, J. Dou, and J. Kim, "Characterization for the vehicle-to-infrastructure channel in urban and highway scenarios at the terahertz band," *IEEE Access*, vol. 7, pp. 166984–166996, 2019.

[49] G R A N W Group et al., "Study on channel model for frequencies from 0.5 to 100 GHz (release 15)," 3GPP TR 38.901, Tech. Rep., 2018.